Unveiling surfaces for advanced materials characterisation with large-area electrochemical jet machining

Alistair Speidel[1], Dongdong Xu[2**], Ivan Bisterov[1,3], Jonathon Mitchell-Smith[3], Adam T. Clare[1*]

[1]Advanced Component Engineering Laboratory, Faculty of Engineering, University of Nottingham, Jubilee Campus, NG8 1BB, UK

[2]Institute for Aerospace Technology, Aerospace Technology Centre, Innovation Park, Triumph Road, Nottingham, NG7 2TU, UK

[3]TextureJet Ltd., 7 Faraday Building, Nottingham Science & Technology Park, Nottingham, NG7 2QP, UK

[*]Corresponding author: adam.clare@nottingham.ac.uk

[**]Corresponding author 2: dongdong.xu@nottingham.ac.uk

Abstract

Surface preparation for advanced materials inspection methods like electron backscatter diffraction (EBSD) generally involve laborious and destructive material sectioning and sequential polishing steps, as EBSD is sensitive to both sample topography and microstrain within the near-surface. While new methodologies, like focussed ion beam and femtosecond laser milling are capable of removing material in a layer-by-layer manner to enable the construction of tomographic datasets within the electron microscope, such techniques incur high initial capital cost for slow removal and reconstruction rates. In this study, ambient condition electrochemical slot jets are applied to rapidly etch (e.g. 31 s) large surface areas (e.g. 160 mm^2) at controlled depths (e.g. 20 µm) with no in-process monitoring. Unveiled surfaces are conducive to measurement by EBSD (raw index rates between 75-95%), despite topographic anisotropy arising both from the process and the material. The mechanisms of topography formation during dissolution under the slot jet are analysed and understood. It is proposed that this slot jet method can be applied to create measurement surfaces for analysis with optical-based microstructural measurement routines reliant on topography and directional reflectance, at a significantly lower cost and time intervention than electron beam-based analysis methods.

Keywords

Electrolyte jet machining, electron backscatter diffraction, indexing, materials characterisation, depth profiling, etching

1.0. Introduction

In high-value manufacturing, there is often a requirement to understand in detail the microstructure and the metallurgy of substrates, specifically at the near-surface, which dictates the safe loading conditions and service lifetimes [1,2]. This is increasingly important considering the drive towards more aggressive operating conditions to maximise component performance in critical applications like turbomachinery for aerospace and land-based power generation [3]. Currently, high-level microstructural analysis is limited by the intervention time and cost penalty, and material wastage. Reducing these factors is necessary to translate high-quality analysis methods from the laboratory to the factory floor, where increases to processing times are unacceptable to industrial operators [4].

Vacuum-based characterisation methods, like electron backscatter diffraction (EBSD), rely on surface preparation steps in order to obtain adequate measurement response. Conventionally, this is achieved through laborious sequential grinding and polishing steps, which are not site-specific and cannot totally eliminate microstrain from the near-surface electron interaction volumes. In practice, microstrain and roughness are often removed by subsequent chemical or electropolishing treatments, enhancing diffraction-based imaging in both EBSD [5], and transmission electron microscopy [6], however it remains challenging to control material removal over a surface. Therefore, methods to prepare surfaces in a more controlled, faster, and less wasteful manner are sought. While sample preparation can in some cases be performed within the electron microscope, for example using Ga^+ and Xe^+ focussed ion beam (FIB) milling [7] and femtosecond laser (FSL) ablation [8], widespread application of these techniques is hampered by high capital and maintenance costs and expert user requirement. When combined with techniques such as EBSD, FIB and FSL preparation methods are ideally suited to singular analysis and can generate intimate 3D tomographic datasets of complex materials [9], however they are largely incompatible with high throughput and low intervention scenarios.

To this end, ambient condition surface characterisation methods, especially those relying on optical [10] and laser ultrasonic inspection [11], are receiving increasing attention due to their potential to increase measurement throughput and as such, be applied throughout multiple areas of manufacturing. As a potential alternative, electrochemical surface preparation enables a high degree of control as material removal is directly proportional to charge transfer, which is readily modulated [12]. Electrochemical preparation is carried out under ambient conditions, where the application of high currents can increase material volumetric removal rates (e.g. 10^6 -10^8 μm^3/s) beyond both FIB and FSL. In addition, electrochemical methods excel at rapidly removing small volumes and the atom-by-atom removal mechanism is understood to impart negligible near-surface stresses upon processing [13,14], for example in

2

comparison to polishing with diamond slurry [15]. These factors make such methods ideal for preparing metallic specimens for further inspection. Surface preparation techniques, such as electrochemical jet machining (EJM), are showing promise towards enabling rapid, high-throughput, and location-specific measurement of microstructural texture [16] and functionalised surface preparation [17].

In the present study, we apply slot jet EJM (Figure 1a-b) to etch large surface areas (e.g. >100 mm^2) for rapid preparation ($\approx$30 s) and analysis. Here, EBSD inspection was chosen as i) it returns a wealth of microstructural information, and ii) EBSD measurement quality is sensitive to material topography and near-surface microstrain, which challenges sample preparation [5]. Aspects of surface processing using slot jet apparatus have been explored, notably with regards to large-area electropolishing [18] and electrochemical turning [19]. However, as a tool to control microscale layer removal and enable the capture of microstructural aspects of the surface, the translational slot jet method is unexplored. Here, we uncover, discuss and address some of the challenges that affect the selective translational etching procedure, thus our present findings aim towards enabling the wider proliferation of the technique as part of an analytical tool.
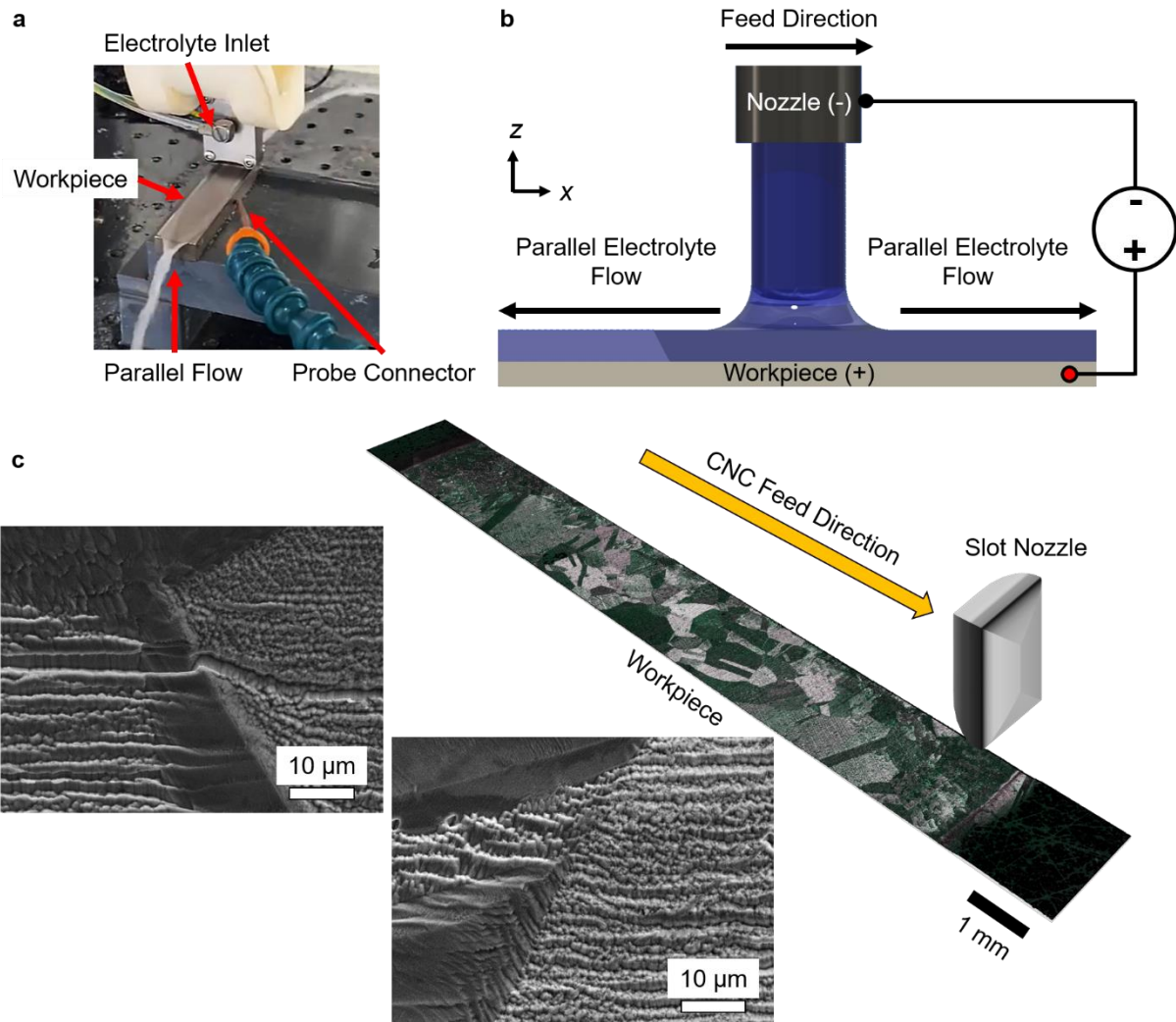
Figure 1: *Unveiling materials with electrochemical jetting. a) Surfaces can be prepared on macroscale components, facilitated by slot jet processing. b) Slot jet etching creates parallel electrolyte flow on impingement. c) Large surface areas can be prepared for further inspection, with grain contrast defined by the orientation-dependent micro-topography.*

2.0. Experimental

2.1. Materials

Commercially pure rolled Ni (Grade 201, Unicorn Metals, UK) was used as the substrate in this investigation (ρ = 8.91 mg/mm^3). Ni was selected as the substrate material to aid conceptualisation, as it generally returns strong Kikuchi patterns in EBSD. Samples of as-received Ni were annealed (1050 °C, 3 hr) to coarsen the grain size and modify the overall grain boundary character to appraise the effect this has on surface generation during etching. The mean grain sizes before (13.2 µm) and after annealing (235.2 µm) were approximated using the linear intercept method from optical micrographs of etched surfaces taken from >200 discrete grains (Figure 2).

4

A greater skew in the scatter of data towards the lower diameters upon annealing is a result of the apparent high density of low energy coherent twin boundaries (CTBs), examples of which are evident in the optical micrograph (Figure 2, inset). A high twinning density is expected in Ni after annealing, which has a relatively low stacking fault energy. Samples of Ni were sequentially ground and polished (to 1 µm diamond), before rinsing with deionised water prior to EJM. The electrolyte was made up with NaCl (Fisher, UK) and deionised water to the required concentration (2.3 M), to form an electrolyte of sufficient electrolytic conductivity to transfer the required charge [16].
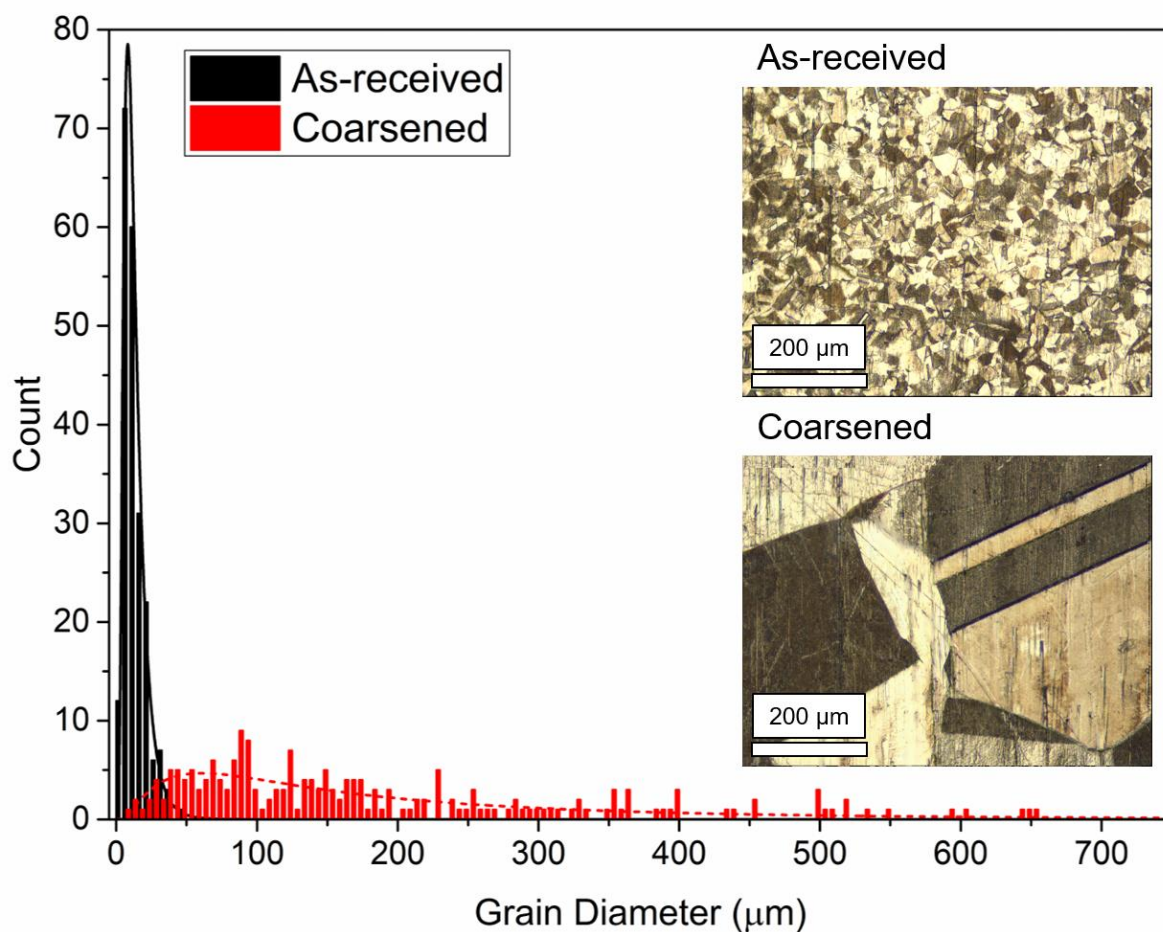

Figure 2: Grain diameter histograms for the as-received and annealed Ni specimens (>200 data points from each specimen), characterised from optical micrographs. Curve is the lognormal of the data distribution. Inset optical micrographs showing the differing grain sizes and character.

2.2.   Electrochemical jet machining approaches

Anodic dissolution is governed by Faraday's laws of electrolysis, which allow relative removal rate predictions, achieved by considering the electrochemical equivalent, eq, for a given material, the mass of a given material liberated by one coulomb of charge:

$$eq = \frac{M_a}{Fz} \qquad [1]$$

where M_a is the atomic mass, F is the Faraday constant (the product of elementary charge and Avogadro's constant), and z the charge number of the reaction. Consideration of material density, ρ, enables prediction of volumetric removal, and etch depth, h:

$$h = \frac{eqQ}{\rho A} \qquad [2]$$

where Q is charge passed, and A is the processed area. Practically, Q is adjusted by control over current and feed rate, v_f. In this study, EJM was performed on a custom-built 3-axis setup (TextureJet Ltd). A slot jet (10.0 x 0.1 mm) was used to modify large surface areas by translation perpendicular to the long slot side. Inter-electrode gap distance (IEG) was maintained at 0.4 mm throughout this study. Jet velocity was 8.15±0.01 m/s unless otherwise stated. Parameters for planar step profiling large areas (160 mm^2) are outlined in Table 1. Total etching time for this sample was 30.6 s, or 0.19 s/mm^2.

Table 1: EJM parameters for step profiling planar etch surfaces. Universal step profiling parameters: step length, l (4.00 mm), applied current, I (2000 mA), feed rate, vf (1.70 mm/s).

Parameter	Layer 1	Layer 2	Layer 3	Layer 4
Target depth, h [µm]	3.97	11.92	15.89	19.87
Passes [n]	1	3	4	5
Cumulative charge, Q [C]	4.71	14.12	18.82	23.53
Areal charge density, Q_A [C/mm^2]	0.118	0.353	0.471	0.588

Alternate EJM approaches were applied to characterise the resulting surface textures in the context of microstructural measurements using electron backscatter diffraction (EBSD). Firstly, a single pass approach was applied to process an area (70 mm^2) at equivalent areal charge density (0.586 C/mm^2) to etch Layer 4 (Table 1), to etch a similar depth (≈20 µm), without sequential processing. This was achieved by applying identical current (2000 mA), but reducing feed rate (0.34 mm/s). Again, the slot jet was translated perpendicular to the nozzle. Total etching time for this sample was 20.5 s, or 0.29 s/mm^2.

Secondly, an orbital etching approach (tidally locked) was applied (Figure 3), wherein a circular motion with a radius of 0.25 mm and circumferential velocity of 2.14 mm/s was superimposed on the nozzle translation along the x-axis (feed rate: 0.34 mm/s, current 2000

mA). Orbital strategies will lead to discontinuous sinusoidal areal charge transfer along the toolpath that will influence local removal rates. Accordingly, the small orbital radius was selected to densely pack nozzle oscillations and homogenise local charge transfer. Areal charge density was maintained as above (0.588 ± 0.012 C/mm^2).
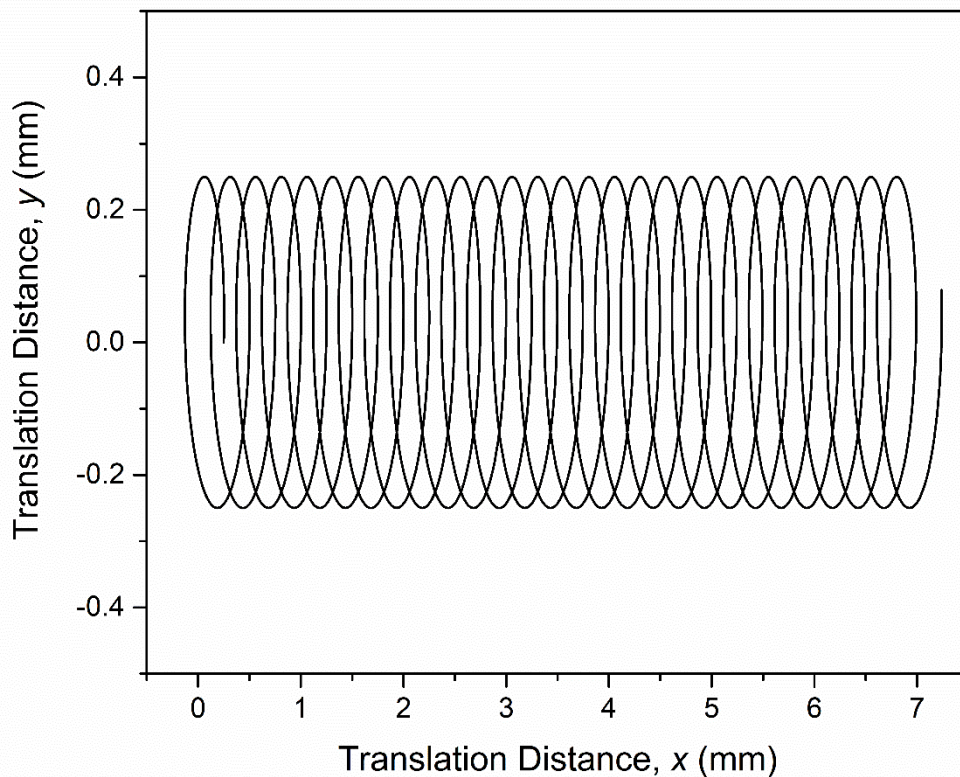

Figure 3: *'Tidally locked' orbital toolpath (radius 0.25 mm, feed rate 0.34 mm/s, current 2000 mA).*

2.3. Characterisation

Etch depths were determined from focus variation microscopy (FVM) datasets (Alicona G4 microscope, 10x objective). The depth of the central 8.5 mm of the 10.0 mm slot was interpreted to account for surface tension effects in slot jet EJM, which affect profile edges [19]. The depth was taken as the mean depth of all of the profiles (1,756) taken across the 1.51 mm width (field of view of the 10x objective), and the error bars are taken as the deviation between the mean depth profile and the best fit line (Supplementary Figure 1).

Surface roughness, *Sq*, and surface-texture aspect, *Str*, were appraised from datasets acquired using the aforementioned FVM (using the higher magnification 100x objective). An 80 μm cut-off filter was applied to the raw surfaces before analysis. Surface texture-aspect

7

ratio is a measure of surface isotropy and is calculated as the ratio between the autocorrelation length and the horizontal distance of the slowest decay of the autocorrelation function to a set value (0.2) [20].

Scanning electron microscopy (SEM) was performed using a Philips XL-30 microscope, and EBSD was performed (Oxford Instruments HKL Advanced) with a field emission electron source (JEOL 7100F, 15 kV). EBSD data acquisition was performed over set areas (600 x 600 µm) and the step size was fixed as 10.00 µm for the coarsened Ni (4.3% of the mean grain diameter); exceptions are explicitly presented in text. EBSD patterns were acquired parallel to and perpendicular to the EJM feed direction (**Figure 4**a-b, respectively). EBSD data were processed using the MTEX toolbox add-on for Matlab (**Figure 4**c indicates map colouring [21]). No filling algorithms were applied to the datasets, and single grain areas were calculated using a 4° misorientation threshold [22]. Local index rates were calculated from the ratio of indexed pixel area in each identified grain (>5 pixel size) to the extracted grain area. Local band contrast values are presented as the mean of the band contrast values for each indexed pixel within the grain.
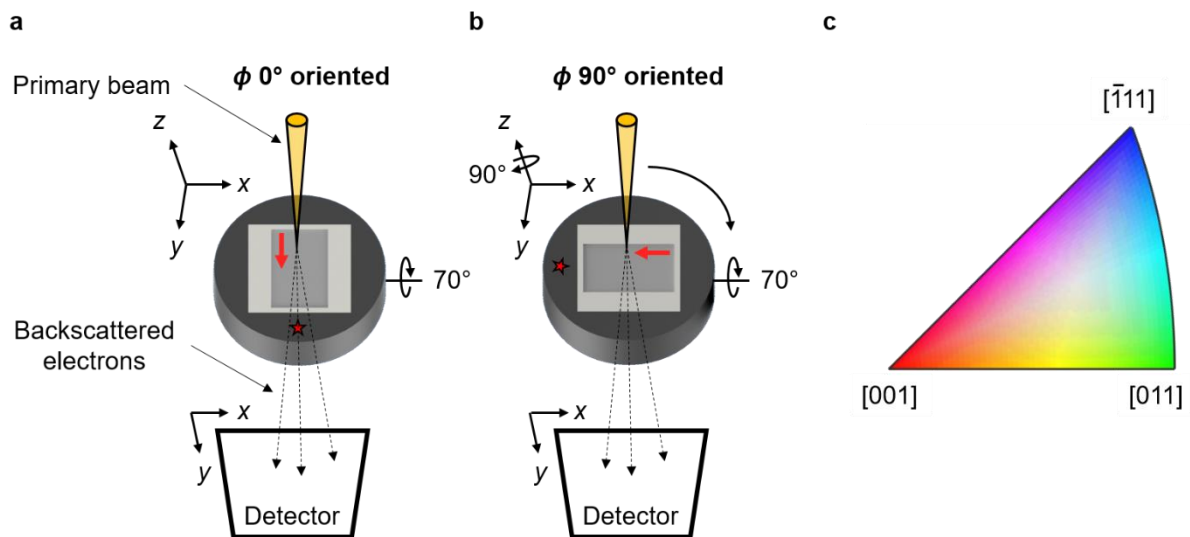

Figure 4: *Sample orientations for EBSD data acquisition within the electron microscope. a) Primary beam oriented parallel (0° oriented) and b) perpendicular (90° oriented) to the feed direction (red arrow). c) Inverse pole figure (z) colouring used for all EBSD orientation maps.*

3.0. Results

3.1. Scratching the surface: ambient planar depth profiling

Stepped layer profiling was applied to prepare large, but site-specific surface areas for inspection, retaining etch depth control. Samples of as-received and coarsened Ni were selectively etched (Table 1), where machined depth was controlled by modulating areal charge

density, by adapting the number of discrete passes at fixed machining parameters. Depth data (Figure 5a) indicate etching proceeds at high current efficiency (as-received: 88-98 %, coarsened: 86-98%). The blue series shows the theoretical removal depth (Eq. 2). High current efficiencies during etching are broadly typical of anodic dissolution in Cl-based electrolytes, where oxygen gas evolution as a side reaction is supressed [23]. The two substrates are compositionally identical, thus display identical behaviour towards the same electrochemical process, demonstrating removal depths are controllable during large-area planar slot jet processing.

An optical micrograph of a section (16 x 6 mm) of the coarsened Ni sample, is shown in Figure 5b. A smaller section of reconstructed surface, acquired using FVM across the translation range of the slot jet (1.5 x 17.0 mm, 10x objective), is shown in Figure 5c, showing the difference in depth upon each successive step. At all areal charge densities, discrete grains can be resolved optically, where contrast is indicative of different surface topographies, dependent on the underlying grain orientation. The etch surfaces appear more reflective at layers with lower areal charge densities and fewer machining passes. Brighter, more reflective etch surfaces are indicative of smoother microscale surface textures. Areas of interest (AOIs) for subsequent EBSD inspection (0.6 x 0.6 mm) are indicated by labelled red boxes inset (*i-iv*) on the etched surface micrograph, accompanied by high-magnification optical micrographs of each area shown in Figure 5*i-v* (polarised light, areas *i-iv*: FVM 50x objective, area v: FVM 100x objective). The green tint in these high-magnification micrographs is indicative of refraction through surface oxide films, which are likely to be formed at low effective current densities, as the slot jet translates away from a given area, while the workpiece is still held at an anodic potential relative to the nozzle. Periodic striations, running parallel to the feed direction can be observed in these high-magnification etch micrographs. Such marks, crossing multiple discretely oriented grains, are an artefact of the etching process.
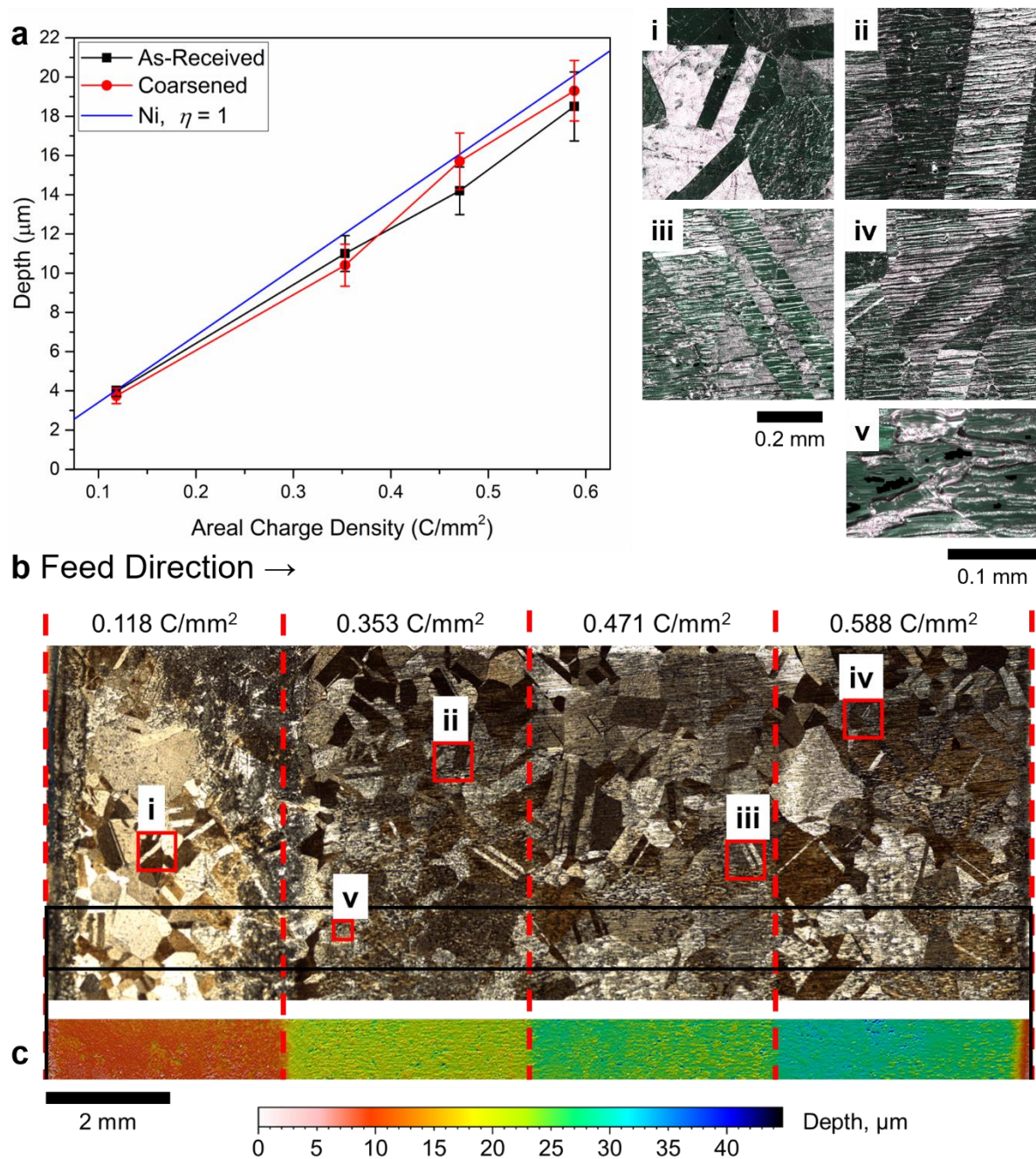
Figure 5: *Electrochemical jetting approaches to step profiling. a) Removal depth is independent of precondition, proceeding at high current efficiency. Blue series calculated from Faraday's law (Eq. 2). Error bars are the average deviation from the line of best fit across the average depth of the central region (1.5 x 8.5 mm) of each processed layer. b) Optical micrograph (unpolarised light) of EJM large-area etch surface in coarsened Ni, showing optical grain contrast, indicative of the underlying topography. i-iv) Extracted areas of interest (polarised light, i-iv: 50x objective, v: 100x objective). c) Surface reconstruction (FVM, 10x objective) showing layer depths.*

3.2. On the relationship between etch topography and EBSD index rate

Topographies of the etched surfaces for both material preconditions were appraised to further understand etch artefact formation and the effect they have on the response rates of further characterisation techniques, such as EBSD. The SE micrographs in Figure 6 show the

development of parallel striations across the separate layers. These appear more pronounced upon successive passes (indicated by higher areal charge density), and occur in both the as-received (Figure 6a-d) and coarsened (Figure 6e-h) specimens. In addition, the effective topographic wavelength, the separation between the discrete striations, appears to be influenced by grain size. For the as-received specimen, the inter-striation distance is smaller than for the coarsened specimen, although the size difference does not appear to scale linearly with grain size in this case. For example, the micrographs in Figure 6b-d show the majority of striations separated by <15 μm, while at the corresponding parameters (Figure 6f-h), the majority of striations in the coarsened sample are separated by <40 μm, in spite of the large difference in mean grain size (13.2 μm to 235.2 μm). Inter-striation separation in this case is challenging to quantify as there is an apparent stochastic element to the development and location of the etch artefacts.

Such differences in topographic height and isotropy can be conveniently characterised by surface metrics including surface roughness, Sq, and surface texture-aspect ratio, Str (Section 2.3). As indicated by the SE micrographs, both samples display similar topographic trends. Concerning roughness (Figure 6i), undulations observed upon successive processing are reproduced in spite of the grain size, where the singular pass (0.118 C/mm^2) generates relatively smooth surfaces in both materials (as-received: 0.22 μm, coarsened: 0.24 μm). However, increasing the number of successive passes increases surface roughness (as-received: 1.21 μm, coarsened: 1.49 μm) after three passes (0.471 C/mm^2). A similar relationship can be observed regarding isotropy indicated by the Str texture-aspect ratio (Figure 6j). At low pass numbers, the surfaces of both materials are more isotropic, while the development of striations increases anisotropy upon multiple passes.
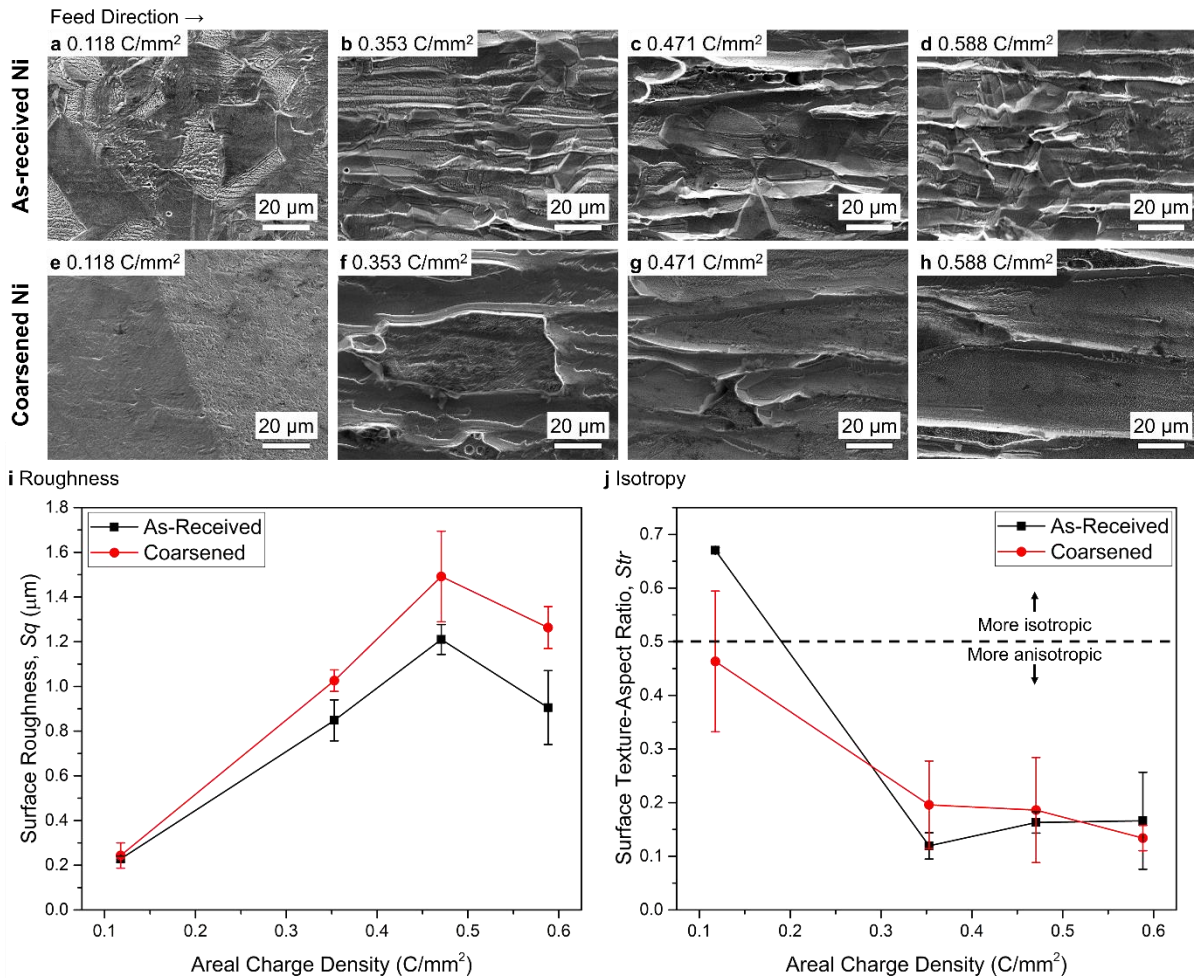
11

Figure 6: *SE micrographs of each surface layer in the as-received (a-d), and coarsened (e-h) samples. Surface roughness, Sq, and surface texture-aspect, Str (isotropy), follow identical trends in both samples. Striation wavelength appears greater in the coarsened sample. Error bars are the standard deviation from the mean of three areas of surface.*

EBSD measurement efficacy (index rate over sampling area) was appraised on these surfaces to understand the effect of the anisotropic etch artefacts. Here, the aforementioned areas of interest on the surface (Figure 5i-iv) were addressed orthogonally, that is to say identical areas were appraised parallel to (arbitrarily termed $\phi = 0°$), and perpendicular to ($\phi = 90°$) the translation direction. This was achieved through a rotation around the z axis (surface normal) in the electron microscope (Figure 4). EBSD measurement quality is sensitive to topographic undulations. A corollary is that the orientation of the anisotropic surface relative to the detector will influence index rate. In this study, a 0.6 x 0.6 mm area was acquired at a step size of 10 µm (<5% of the mean grain diameter for the coarsened Ni).

The orthogonal EBSD results are presented in Figure 7a-b, with the topography of each exemplar area presented in Figure 7c (grain boundaries extracted from EBSD data). For both sample orientations, there is an appreciable decline in successful index rate upon repeated passes (0° oriented 0.118 C/mm^2: 91.7%, 0.471 C/mm^2: 82.8%). In both cases, this correlates

with the *Sq* and *Str* results (Figure 7d-e), showing the sensitivity of EBSD to etched surface quality. No data post-processing operations, like de-noising or filling, were applied to the datasets (Figure 7a-b).

Upon sample rotation to $\phi = 90°$ (translation direction perpendicular to the incident electron beam), there is a moderate decline in index rate for the anisotropic multiple pass layers (area of interest ii: 12%; iii: 6%; iv: 4%), and no decrease for the isotropic single pass layer (area of interest i). Furthermore, zero solution areas of the EBSD datasets (black pixels) can be spatially correlated with topographic aberrations, specifically in areas where the surface profile is skewed towards height and depth extremes, shown in the surface reconstructions (Figure 7c). Relatively large surface undulations shadow the areas on the adjacent slopes on the side of the incident beam, leading to data loss as successfully diffracted electrons cannot reach the detector and therefore cannot be indexed (Figure 7f). Where the striations are aligned parallel to the incident beam, shadowing is reduced and index rate increases (Figure 7g).

Ultimately, that anisotropic surfaces lead to anisotropic EBSD measurement success is largely unsurprising. Despite this, even with samples oriented with artefacts perpendicular to the incident beam, where shadowing effects are likely to be enhanced, individual grains can be resolved at an appropriate resolution for this material. The atom-by-atom mechanism of electrochemical etching is assistive in generating surfaces conducive to measurement, free from microstrain, despite topographic anomalies. Additionally, these results should be considered in the context of the small cumulative processing time (<31 s) required to etch the entire sample surface (160 mm^2) across multiple, controlled depths (Layer 1: 2.35 s; Layer 2: 7.06 s; Layer 3: 9.41 s; Layer 4: 11.76 s).

When etching fine grained samples at these parameters, there is likely to be a grain size limit below which the slot jet preparation method may struggle to generate surfaces conducive to EBSD measurement, especially where the striations approach the grain size. However, it should be noted that i) striation separation reduces with grain size, and ii) the *Sq* roughness is marginally lower for the finer grained sample (Figure 6i), both of which may reduce this dependence. These preparation times appear favourable when compared with conventional EBSD surface preparation methods, for example successive grinding, diamond polishing, colloidal silica polishing, and vibratory finishing steps [24]. Thus, it is considered that when applied appropriately, EJM can dramatically increase the throughput of what is generally considered a *low-throughput-high-quality surface* analysis technique in a site-specific manner.
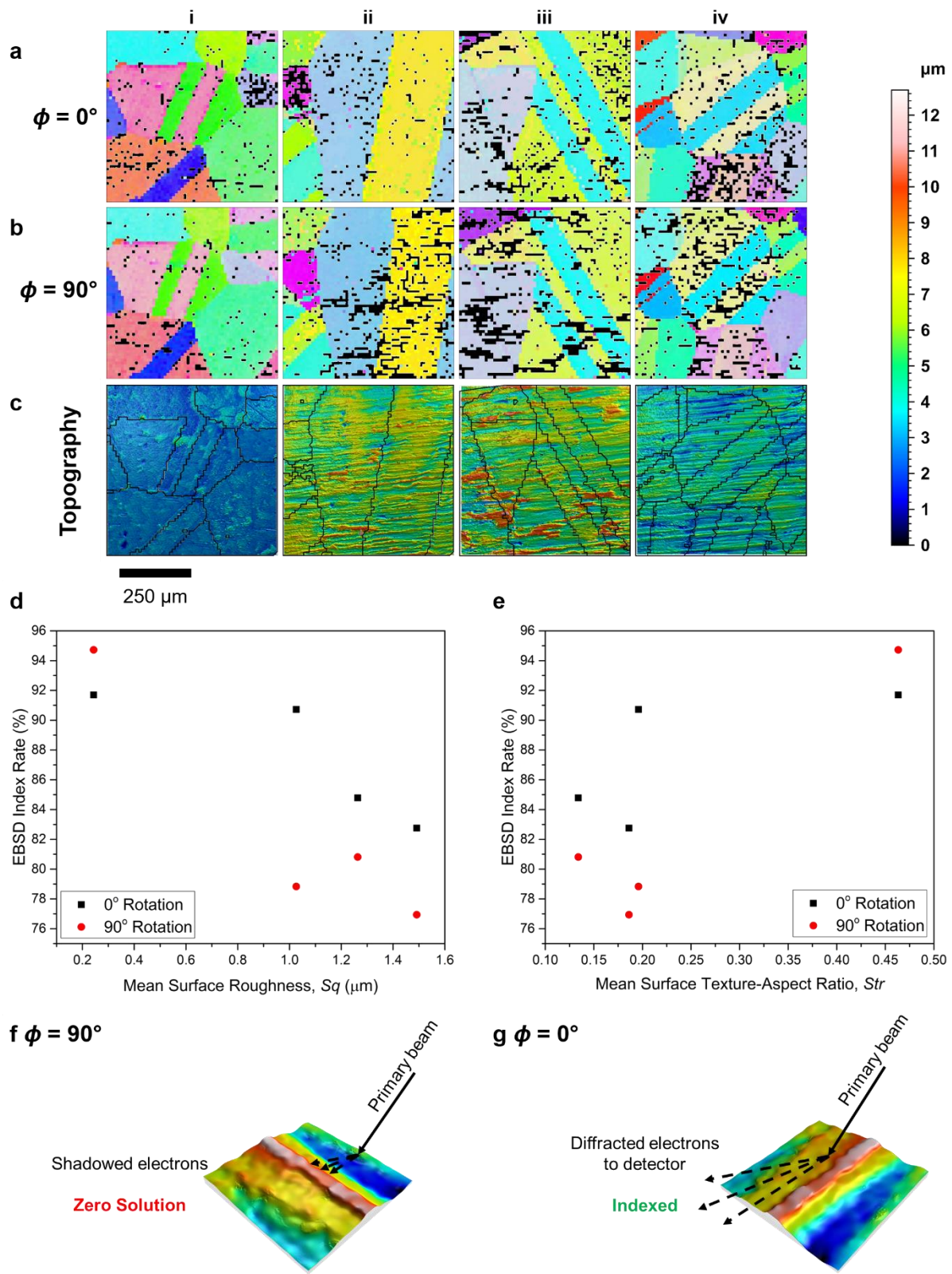
Figure 7: *EJM surface anisotropy affects the index rate in EBSD studies. a) EBSD data (0.36 mm², 10 µm pixel size) acquired from areas of interest i-iv on the coarsened Ni with striations oriented parallel to the incident beam. b) EBSD acquired under identical conditions of identical areas of interest, with the sample orientation rotated through 90°. See IPF for colouring. c) EBSD zero solution can be spatially correlated with topographic extremes (see grain boundary overlay), see height scale for reference to colour. Index rate is lower where incident beam is 90° with respect to translation direction. d) This is inversely correlated to Sq roughness, and e) positively correlated*

3.3. On the origins and propagation of translational artefacts

The EJM etch artefacts are dependent on both the material microstructure and the translation of the electrolyte jet. The latter is evidenced by the anisotropy of the etch surfaces, with striations running parallel to the translation direction, crossing multiple grain boundaries. Evidence to support the former is given in the correlative study Figure 8, showing area of interest 'v' upon etching (Figure 5 for location). The secondary electron image (Figure 8a) shows this area of interest, where the largest red box indicates the area of FVM topography acquisition (Figure 8b). The surface profile shows deep trench features in this field of view with approximately ≈5-7 μm of height difference from the top surface. Again, these trench features are oriented approximately parallel to the feed and flow directions.

The acquired EBSD dataset for this field of view, acquired at 90° sample rotation relative to the detector (Figure 8c), shows poor indexing in areas correlating with the raised topography (0.25 x 0.15 mm field of view, 2.5 μm step size). This leads to the shadowing of diffracted electrons from the detector, following a mechanism similar to that indicated in Figure 7f. The SE micrographs indicate firstly that the striations are likely to be initiated by discrete crystallographic pits, such as the clusters observed Figure 8d. Where there is a vector of nozzle translation or electrolyte flow, pits are propagated parallel to this direction. Previously, discrete pitting events have been shown to be directionally propagated by nozzle translation in EJM, for example in Ti-alloys using certain electrolytes [25]. Such pits are likely to be initiated at points of local microstructural inhomogeneity like certain grain boundaries, or discontinuities in the native oxide layer, which provides passive corrosion protection. Secondly, it can be seen that upon propagation, the etch pits retain similarly oriented etch facets, and these can be propagated across grain boundaries, to create larger scale striations (Figure 8e). While the macroscale striation is retained in spite of the grain boundary, the specific orientations of the revealed etch facets are different across the grain boundary.
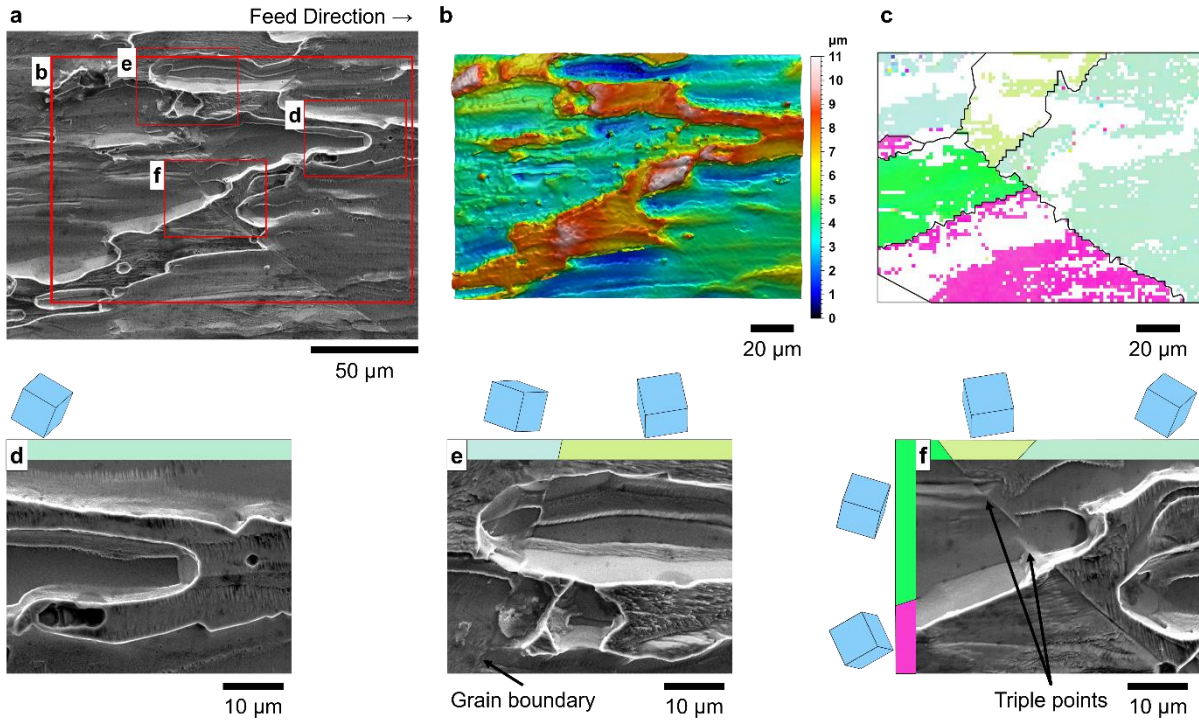
Figure 8: *Striation geometries are bounded by crystalline etch facets. a) SE micrograph of area of interest v, inset boxes showing acquistion areas of further microscopic study. b) Topography reconstruction (FVM, 100x objective) of area of interest v showing relatively large height differences across the striations. c) Areas of EBSD zero solution (white pixels) are spatially correlated with topographic aberrations. d-f) Micrographs show striations are bounded by anisotropic etch facets, propagating these facets leads to striation development across multiple grains and triple points.*

Determining the dominant factor in etch artefact formation is complicated by jet translation and electrolyte flow following the same axis (Figure 1b). To isolate these factors, it is necessary to observe features etched without translation, such as the termination regions, where the feed starts and stops, and static nozzle etching operations. The latter will return the footprint of the jet (jet analogue of a beam footprint [26]). The optical micrographs in Figure 9a show the starting and termination regions of a single pass toolpath in coarse-grained Ni (Section 2.3), with approximate locations of the toolpath start and end points marked by dashed boxes. Striations occur beyond these areas. SE micrographs show the initiation of discrete pits within and beyond the termination region, which occur at defects like grain boundaries (Figure 9b). The propagation of an artefact from a pitting event ahead of the jet is shown in Figure 9c, indicating striation growth is influenced by electrolyte flow. Multiple discrete pits form ahead of the jet, from which the striations arise (Figure 9d). Figure 9e shows a static etching operation in as-received Ni (2.00 A, 5 s dwell), where the striations occur parallel to the flow, which is radial at the extremes of the drilled slot. The effect of flow on the etch textures was determined by modifying the jet velocity in these static jetting scenarios. The optical micrographs (Figure 9f-h) indicate a reduction in the striation magnitude as jet velocity is increased (5.91 - 10.24 m/s) at the exposed surface etched without translation.

Pit initiation here is consistent with corrosion studies, originating at surface defects, aligning with certain grain boundaries [27] and pre-existing grind marks [28]. In these pits, the surface is locally de-passivated, revealing anisotropic morphologies dictated by remnant slow etch surfaces. It is understood that increasing flow efficiency encourages the removal of electrochemical reactant products from the sample surface, preventing the accumulation of anodic films and the development of the mass transport limited condition [29]. These films can dissociate material removal from the underlying microstructure; conversely, efficient evacuation of these films will promote the anisotropic etching condition. Accordingly, it is intuitive that the striation artefacts are likely to channel the flow of electrolyte parallel to the surface, enhancing the local removal efficacy of reactant products (Figure 9i-j). This would allow striation propagation as i) high local flow efficiencies would promote local material removal parallel to the flow, ii) which in turn further channels local electrolyte flow. Successive passes over the same regions will likely exploit the same striation channels. Thus, the superimposition of striations would increase roughness amplitude and anisotropy upon repeated passes. That the increase in jet velocity reduces striation formation is likely a result of greater evacuation conditions over the surface, independent of etch facets that disrupt electrolyte flow at lower jet velocities.
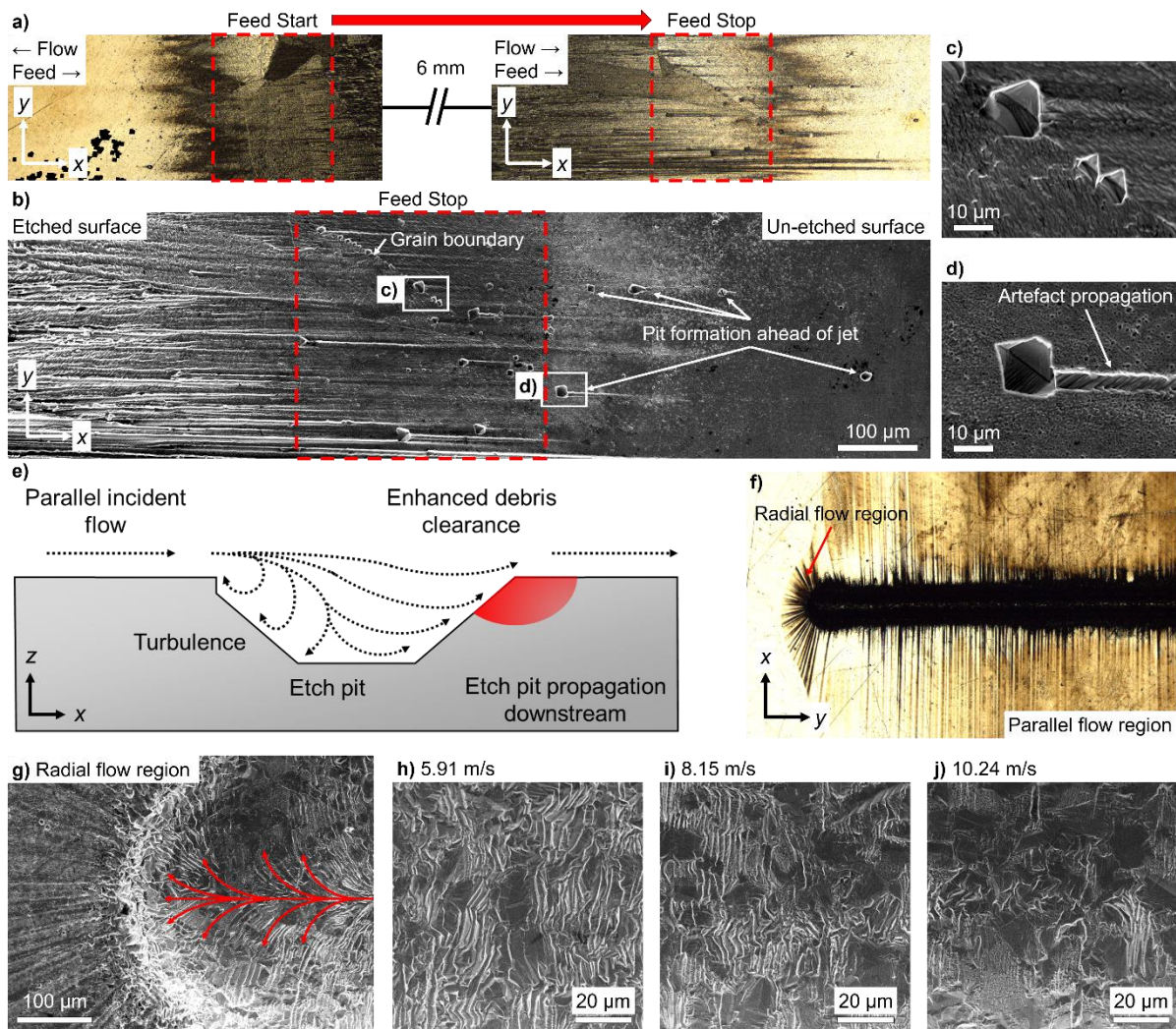
Figure 9: *Striations propagate from pits ahead of the jet. Translation and electrolyte flow follow axis 'x'. a) Optical micrographs showing jet termination regions after single pass processing. b) SE micrographs showing the nucleation of pit features on discontinuities, c) like grain boundaries. d) Striations propagate from these pits, parallel to the electrolyte flow, ahead of the jet. e) Flow is more complex within pits than flat surfaces generating differential flow conditions downstream of the pit where greater film clearance rates are likely to propagate the pits. f) In static etching (no translation), striations propagate from the etched slot, g) including radially at the slot ends. h-j) Increasing flow velocity reduces striations at the etched surface at these parameters (5.91, 8.15, and 10.24 m/s, respectively).*

3.4. Processing challenges: reducing repeats or orbital machining?

The processing approach required to overcome characteristic etch striations depends on the magnitude of the depth to be etched, and the surface inspection strategy to be used after EJM. In this section, different approaches are explored to etch a given depth of material (≈20 μm), and the resulting surface quality in relation to the applicability to EBSD measurement is discussed. In the case that the striation amplitude is increased upon repeated passes, the facile route through which one might reduce these striations is by reducing the number of repeated passes to achieve a given depth. For a given current density condition, this is achieved by reducing nozzle feed rate, v_f. As such, coarse Ni was processed at equivalent

areal charge density to the multi-pass Layer 4 outlined in Table 1 (0.586 C/mm^2), to etch the same depth in a single pass, at a lower feed rate (v_f = 0.34 mm/s), at the same applied current (2000 mA). The resulting mean profile depth, h (19.5 ±1.4 µm), is within the error range of Layer 4 in the coarsened sample (19.3 ±1.5 µm), and the theoretical value (19.9 µm) calculated according to Eq. 2.

However, the single pass approach to surface preparation is not suitable for all further inspection strategies. Firstly, where there is a desire to profile microstructure through the depth of a sample, akin to tomography, repeated passes are necessary as part of a rapid *etch-inspect-etch-inspect* strategy to build up discrete layers of information. Secondly, it should be noted that slower feed rates could enable the development of high surface concentrations of oxides, as freshly etched surface areas are held at high potential, low current density conditions for longer times. This may affect both optical-based inspection methods if i) surface reflectivity or ii) hue changes, and EBSD if the anodic oxide layer i) develops crystallinity, or ii) becomes too thick. Thus, where there is a desire to etch large material volumes for inspection, single pass processing is unlikely to provide adequate results and more advanced etching approaches are required.

Processing approaches that change the electrolyte flow direction and the translation vector are likely to prevent striation formation. Simply changing translation vector is ineffective at eliminating these artefacts, as electrolyte flow axis is unchanged. This was appraised by processing coarse Ni using an orbital toolpath to change the translation vector (Figure 3b) at 0.34 mm/s feed rate. The similar topographic anisotropy between the Layer 4 multi-pass sample: Figure 10a (*Str* = 0.134 ±0.024), the single pass sample: Figure 10b (*Str* = 0.261 ±0.084), and the orbital pass sample: Figure 10c (*Str* = 0.256 ±0.119) are quantitative indicators that the presence of striated etch artefacts is not a result of repeat processing or solely the translation vector.

Striation amplitude is reduced upon single-pass processing, indicated by the lower *Sq* roughness of this sample (0.35 µm ±0.07 µm) compared with the Layer 4 multi-pass in the same material, shown in Figure 6i (1.26 ±0.09 µm). However, the orbital approach does not show the same reduction in roughness (1.03 ±0.42 µm). That the striation amplitude is greater upon multiple passes appears to be caused by a compounding or summation effect. Etch facets in pitting are defined by relative dissolution rates of the different crystallographic planes. The origin of these pitting events is likely to have a stochastic relationship to a number of factors, for example the distribution of defects in the material. Once a discrete pit has been initiated, propagated and halted (Figure 8d) during a preceding machining pass, subsequent etching appears to preferentially attack these regions where the local corrosion resistance has

19

been degraded and the electrolyte flow can be channelled, further focussing etching in these locations. The surface amplitude increases, and the anisotropy defined by the flow and the orientation-dependent etch rates is retained. Considering the orbital processing approach, the higher roughness likely results from the undulating charge density associated with the orbital jetting strategy, specifically where the retrograde nozzle motion will promote material removal in pre-existing channels, analogous to repeated passes, leading to deeper striations.

Figure 10e-f shows EBSD maps acquired at 0° and 90° to the nozzle translation direction for the single pass, and orbital pass approach (Figure 10h-i), respectively (0.36 mm^2, 10 µm^2 pixel size). Both datasets show a reduction in index rate on sample rotation perpendicular to the striation direction (single pass: 92 % to 77 %, orbital pass: 82 % to 70 %), as surface anisotropy is retained throughout all processing strategies. The difference in index rates between these samples can be understood through observing etch topographies (Figure 10 grains: 1-3 single pass; 4-7 orbital pass), where topographies are finer than those resulting from the orbital pass. This is likely due to the aforementioned retrograde motion that will lead to charge accumulation and promotion of material removal in pre-existing etch pits. Both datasets indicate an orientation dependence of index rate at these etching parameters. For example, grains 1 and 3 show index rates of 98% and 95% respectively, while within grain 2, a 59% index rate is achieved where the sample is 0° orientated. Index rates are lower for each of these grains in the 90° acquisition orientation.
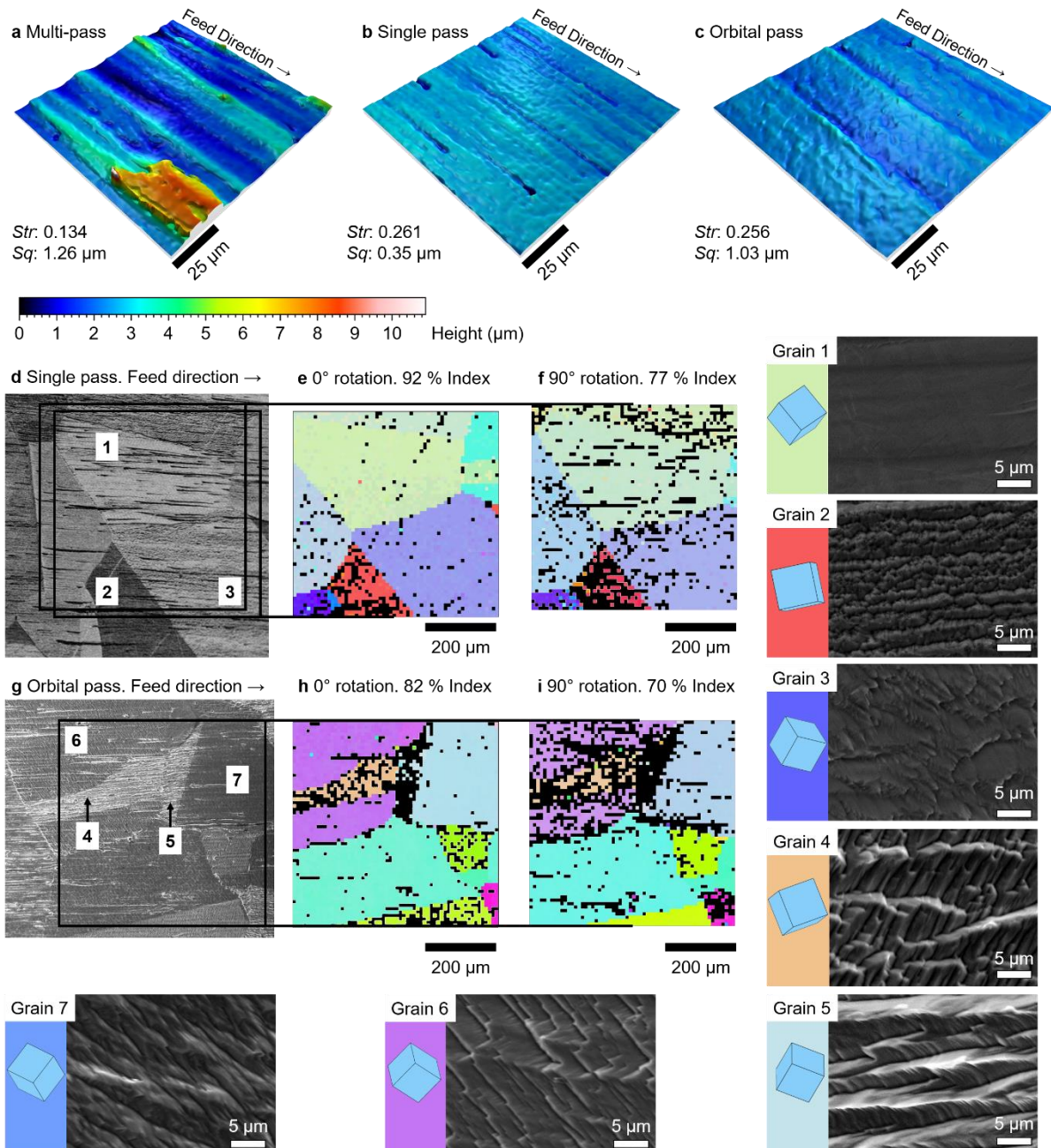
Figure 10: *Processing strategy changes topography in 20 µm depth removal. a) Multi-pass approach (5 passes), b) Single-pass approach, c) orbital pass approach. d) FSD image of the single pass surface, showing orthogonal EBSD acquisition areas (HSV colouring), e) at 0° (primary beam parallel to feed), f) at 90° (primary beam perpendicular to feed). g) SE image of orbital pass surface, showing EBSD acquisition areas h) at 0° and i) at 90°. SE micrographs of grains 1-7 showing increasing scale of topography on orbital etching. <100> oriented grains show lower index rate, correlating with the complex surface.*

3.5. On orientation-dependent index rates

Orientation-dependent index rates are intuitive given the anisotropic etch topographies and the surface sensitivity of EBSD. To quantify this dependency, a larger acquisition area (≈8 mm², 3.29 x 2.42 mm) was measured by EBSD to sample a more statistically relevant number of grains at the same acquisition parameters (10 µm step size). In this study, the single pass

21

approach was applied to remove ≈20 µm of material (0.586 C/mm^2) to minimise striation amplitude of and the EBSD dataset was acquired in the 0° sample orientation, parallel to the nozzle feed direction to maximise index rates.

Figure 11a shows the resulting map with a global index rate of 92%, correlating with Figure 10h (etched at the same parameters), with the associated band contrast map of the data (Figure 11b). Mean angular deviation (MAD) data indicates no strong correlation with material or topography (Supplementary Figure 2). The inverse pole figure (IPF, z direction) in Figure 11c shows the scatter of data from this set. Regions of high data density are indicative of discrete grains. To appraise the dependence of index rate on orientation, the data were separated into individual grains (4° misorientation threshold), where Figure 11a shows the resulting grain boundary overlay. Individual grains were plotted on the resulting IPF (Figure 11d, marker area scaled to grain area). Local grain-averaged index rates were plot onto the IPF (Figure 11e), showing the spread in index rates (45-100%). As indicated in Figure 10h-i, grains oriented towards <001> directions tend towards lower index rates. This is intuitive, as after etching, orientations aligned towards <001> are typically characterised by inverted square pyramidal morphologies (Grain 2, Figure 10), rather than plateaued regions (Grains 1 and 3, Figure 10), which tend not to shadow backscattered electrons.

Both in-grain effects and the etching process drive differences in band contrast across the dataset. Data shows slight positive correlation (Pearson's R^2 = 0.56) between grain-averaged index rate and grain-averaged band contrast (Figure 11f), where it is known that band contrast is influenced by grain orientation. Differences in band contrast also arise over multiple grains, following the feed direction. Band contrast periodicity in the data is exemplified in AOI *vi* (red rectangle Figure 11a). Figure 11g shows the associated orientation data (IPF colouring), Figure 11h the band contrast, Figure 11i the corresponding optical micrograph, and Figure 11j the FVM topography map for AOI *vi*. Here, index rates and band contrast values are correlated to both orientation and the feed direction. For example, large non-indexed areas are associated with low band contrast in the surrounding regions, appearing in <001>-aligned grains. Likewise, the recessed striation (demarcated by arrows, Figure 11g-j) returns comparatively good indexing, and relatively high band contrast values, despite transiting the same <001> aligned grains. It is considered that while the index rate success and pattern quality is a function of the grain orientation, this effect is exacerbated by the parametric influence of the electrolyte flow at the sample surface. These agree with findings that band contrast and pattern quality variation are related to sample topography [30]. Variations in MAD do not correlate readily with topography, although there is some apparent grain dependence (Supplementary Figure 3), while the global correlation between grain-averaged index rate and MAD is not strong (Pearson's R^2 = -0.22) (Supplementary Figure 4).
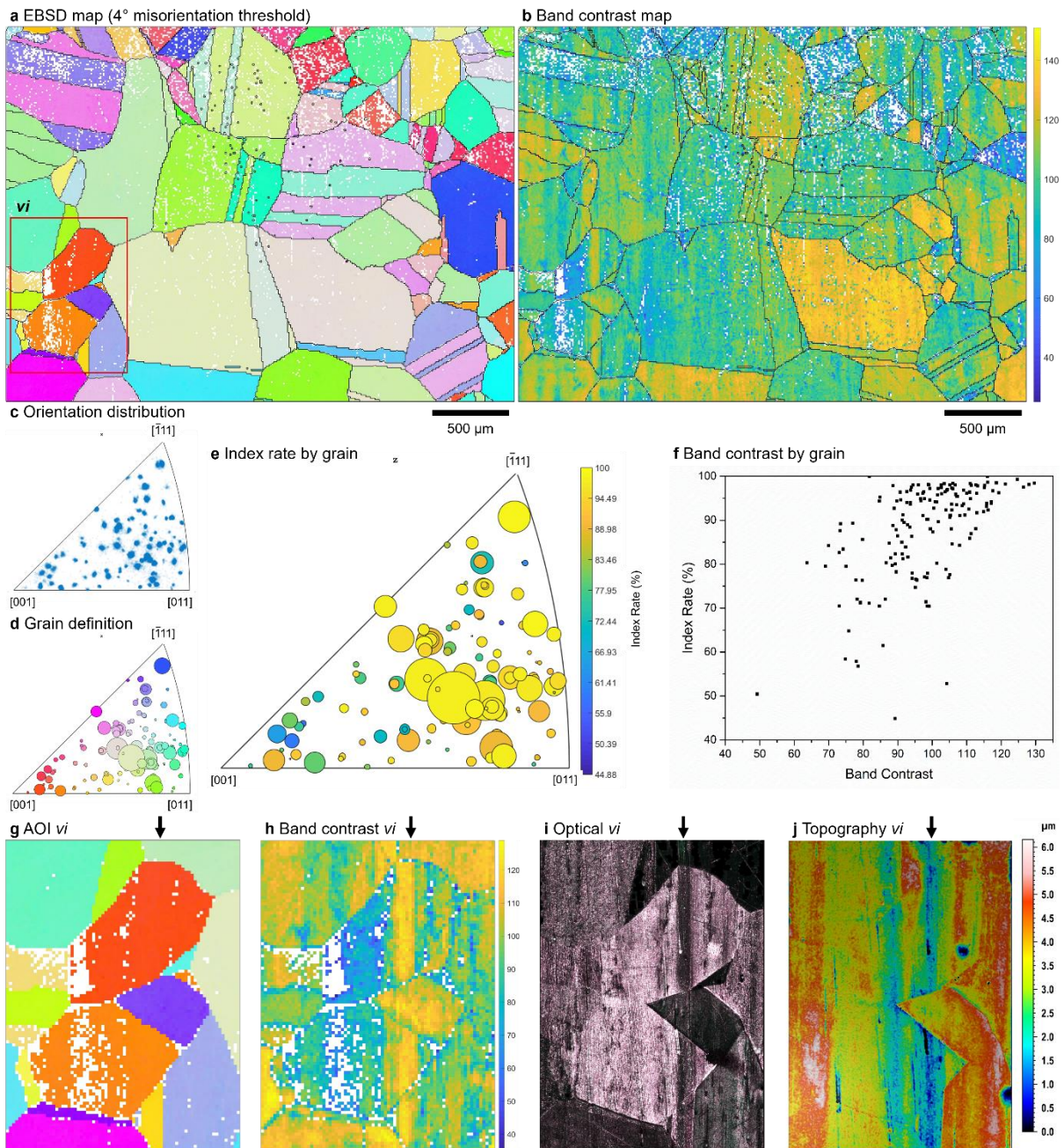
Figure 11: a) Large area (≈8 mm²) EBSD map acquired from the single pass surface (20 μm depth from top surface). Grain boundaries identified from >4° of local misorientation (>5 pixels). b) Corresponding band contrast map. c) IPF (z) showing the scatter of data from the map area. Agglomerations are indicative of single grain regions. d) IPF (z), with markers scaled to grain areas. e) IPF (z) (index rate colouring) of the discretised single grain regions, f) slight correlation between grain-isolated band contrast and grain-isolated index rates. Area of interest vi: g) EBSD (IPF) data, h) band contrast data, i) optical micrograph, and j) topography data. Index rate varies across single grain areas.

Considering process-induced anisotropy, the flow-generated striations, predominantly caused by differential flow regimes over the surface, appear to be reduced by equalising electrolyte flow. Practically, this is achieved by increasing the jet velocity. Considering material-induced anisotropy, the scale of the etch facets can be reduced by increasing the applied current density at the surface, where the removal mechanism tends towards electropolishing. However, it should be noted that for orientation measurement routines reliant on topography

[16], or directional reflectance from etch facets [10,31], anisotropic etch textures may be beneficial.

4.0. Conclusions

In this study, we have introduced EJM as a route through which large-area (e.g. 160 mm^2) surfaces can be prepared in a depth-controlled manner for subsequent inspection using advanced characterisation methods such as EBSD. Surfaces were prepared rapidly (e.g. <0.3 s/mm^2) and were shown to be compatible with EBSD measurement. EBSD measurement quality (index rate) is shown to deteriorate upon multiple passes to etch a defined volume of material, although for a large sampling area (e.g. 0.36 mm^2), index rate does not deteriorate below 77% at the acquisition parameters applied in this study, and individual grains can be identified and studied. The surface texture created by EJM is shown to be anisotropic due to the propagation of discrete crystallographic pitting events, and this influences the EBSD index rate. Where surfaces are prepared by EJM using etching parameters, it is recommended that EBSD inspection is performed parallel to the feed direction (and therefore striation direction) when samples are prepared with a multi-pass approach.

5.0. Acknowledgements

The raw/processed data required to reproduce these findings cannot be shared at this time as the data also forms part of an ongoing study.

6.0. References

[1]   A. Thakur, S. Gangopadhyay, State-of-the-art in surface integrity in machining of nickel-based super alloys, Int. J. Mach. Tools Manuf. 100 (2016) 25–54. https://doi.org/10.1016/j.ijmachtools.2015.10.001.

[2]   Z. Liao, A. Abdelhafeez, H. Li, Y. Yang, O.G. Diaz, D. Axinte, State-of-the-art of surface integrity in machining of metal matrix composites, Int. J. Mach. Tools Manuf. 143 (2019) 63–91. https://doi.org/10.1016/j.ijmachtools.2019.05.006.

24

[3]   J.H. Perepezko, The Hotter the Engine, the Better, Science (80-.). 326 (2009) 1068–1069. https://doi.org/10.1126/science.1179327.

[4]   J.M. Allwood, T.H.C. Childs, A.T. Clare, A.K.M. De Silva, V. Dhokia, I.M. Hutchings, R.K. Leach, D.R. Leal-Ayala, S. Lowth, C.E. Majewski, A. Marzano, J. Mehnen, A. Nassehi, E. Ozturk, M.H. Raffles, R. Roy, I. Shyha, S. Turner, Manufacturing at double the speed, J. Mater. Process. Technol. 229 (2015) 729–757. https://doi.org/10.1016/j.jmatprotec.2015.10.028.

[5]   G.L. Wynick, C.J. Boehlert, Use of electropolishing for enhanced metallic specimen preparation for electron backscatter diffraction analysis, Mater. Charact. 55 (2005) 190–202. https://doi.org/10.1016/j.matchar.2005.04.008.

[6]   N. Ünlü, Preparation of high quality Al TEM specimens via a double-jet electropolishing technique, Mater. Charact. 59 (2008) 547–553. https://doi.org/10.1016/j.matchar.2007.04.003.

[7]   J. Liu, R. Niu, J. Gu, M. Cabral, M. Song, X. Liao, Effect of Ion Irradiation Introduced by Focused Ion-Beam Milling on the Mechanical Behaviour of Sub-Micron-Sized Samples, Sci. Rep. 10 (2020) 10324. https://doi.org/10.1038/s41598-020-66564-y.

[8]   M.P. Echlin, M.S. Titus, M. Straw, P. Gumbsch, T.M. Pollock, Materials response to glancing incidence femtosecond laser ablation, Acta Mater. 124 (2017) 37–46. https://doi.org/10.1016/j.actamat.2016.10.055.

[9]   A.T. Polonsky, M.P. Echlin, W.C. Lenthe, R.R. Dehoff, M.M. Kirka, T.M. Pollock, Defects and 3D structural inhomogeneity in electron beam additively manufactured Inconel 718, Mater. Charact. 143 (2018) 171–181. https://doi.org/10.1016/j.matchar.2018.02.020.

[10]   M. Seita, M.M. Nimerfroh, M.J. Demkowicz, Acquisition of partial grain orientation information using optical microscopy, Acta Mater. 123 (2017) 70–81. https://doi.org/10.1016/j.actamat.2016.10.021.

[11]   P. Dryburgh, R.J. Smith, P. Marrow, S.J. Lainé, S.D. Sharples, M. Clark, W. Li, Determining the crystallographic orientation of hexagonal crystal structure materials with surface acoustic wave velocity measurements, Ultrasonics. 108 (2020) 106171. https://doi.org/10.1016/j.ultras.2020.106171.

[12]   K.K. Saxena, J. Qian, D. Reynaerts, A review on process capabilities of electrochemical micromachining and its hybrid variants, Int. J. Mach. Tools Manuf. 127 (2018) 28–56. https://doi.org/10.1016/j.ijmachtools.2018.01.004.

[13]   W. Han, F. Fang, Fundamental aspects and recent developments in electropolishing, Int. J. Mach. Tools Manuf. 139 (2019) 1–23. https://doi.org/10.1016/j.ijmachtools.2019.01.001.

[14]   Z. Liao, A. la Monaca, J. Murray, A. Speidel, D. Ushmaev, A. Clare, D. Axinte, R. M'Saoubi, Surface integrity in metal machining - Part I: Fundamentals of surface characteristics and formation mechanisms, Int. J. Mach. Tools Manuf. 162 (2021) 103687. https://doi.org/10.1016/j.ijmachtools.2020.103687.

[15]   J. Everaerts, E. Salvati, A.M. Korsunsky, Nanoscale Depth Profiling of Residual Stresses Due to Fine Surface Finishing, Adv. Mater. Interfaces. 6 (2019) 1900947. https://doi.org/10.1002/admi.201900947.

[16]   A. Speidel, R. Su, J. Mitchell-Smith, P. Dryburgh, I. Bisterov, D. Pieris, W. Li, R. Patel, M. Clark, A.T. Clare, Crystallographic texture can be rapidly determined by electrochemical surface analytics, Acta Mater. 159 (2018) 89–101. https://doi.org/10.1016/j.actamat.2018.07.059.

[17]   A. Speidel, J.W. Murray, I. Bisterov, J. Mitchell-Smith, C. Parmenter, A.T. Clare, Thermal Activation of

Electrochemical Seed Surfaces for Selective and Tunable Hydrophobic Patterning, ACS Appl. Mater. Interfaces. 12 (2020) 7744–7759. https://doi.org/10.1021/acsami.9b20121.

[18] T. Kawanaka, M. Kunieda, Mirror-like finishing by electrolyte jet machining, CIRP Ann. 64 (2015) 237–240. https://doi.org/10.1016/j.cirp.2015.04.029.

[19] M. Kunieda, K. Mizugai, S. Watanabe, N. Shibuya, N. Iwamoto, Electrochemical micromachining using flat electrolyte jet, CIRP Ann. 60 (2011) 251–254. https://doi.org/10.1016/j.cirp.2011.03.022.

[20] R. Leach, ed., Optical Measurement of Surface Topography, Springer Berlin Heidelberg, Berlin, Heidelberg, 2011. https://doi.org/10.1007/978-3-642-12012-1.

[21] G. Nolze, R. Hielscher, Orientations – perfectly colored, J. Appl. Crystallogr. 49 (2016) 1786–1802. https://doi.org/10.1107/S1600576716012942.

[22] F. Bachmann, R. Hielscher, H. Schaeben, Grain detection from 2d and 3d EBSD data—Specification of the MTEX algorithm, Ultramicroscopy. 111 (2011) 1720–1733. https://doi.org/10.1016/j.ultramic.2011.08.002.

[23] M.M. Lohrengel, K.P. Rataj, T. Münninghoff, Electrochemical Machining—mechanisms of anodic dissolution, Electrochim. Acta. 201 (2016) 348–353. https://doi.org/10.1016/j.electacta.2015.12.219.

[24] M.M. Nowell, R.A. Witt, B. True, EBSD Sample Preparation: Techniques, Tips, and Tricks, Microsc. Microanal. 11 (2005). https://doi.org/10.1017/S143192760550672X.

[25] A. Speidel, J. Mitchell-Smith, I. Bisterov, A.T. Clare, Oscillatory behaviour in the electrochemical jet processing of titanium, J. Mater. Process. Technol. 273 (2019) 116264. https://doi.org/10.1016/j.jmatprotec.2019.116264.

[26] G.E. Ozur, V.P. Grigor'ev, K. V. Karlik, T. V. Koval', L.H. Dung, Shaping of the cross section of a nonrelativistic high-current electron beam by means of return current leads, Tech. Phys. 56 (2011) 1320–1324. https://doi.org/10.1134/S1063784211090179.

[27] S.K. Pradhan, P. Bhuyan, S. Mandal, Influence of the individual microstructural features on pitting corrosion in type 304 austenitic stainless steel, Corros. Sci. 158 (2019) 108091. https://doi.org/10.1016/j.corsci.2019.108091.

[28] L. Wei, Y. Liu, Q. Li, Y.F. Cheng, Effect of roughness on general corrosion and pitting of (FeCoCrNi)0.89(WC)0.11 high-entropy alloy composite in 3.5 wt.% NaCl solution, Corros. Sci. 146 (2019) 44–57. https://doi.org/10.1016/j.corsci.2018.10.025.

[29] D. Landolt, Fundamental aspects of electropolishing, Electrochim. Acta. 32 (1987) 1–11. https://doi.org/10.1016/0013-4686(87)87001-9.

[30] S.I. Wright, M.M. Nowell, EBSD Image Quality Mapping, Microsc. Microanal. 12 (2006) 72–84. https://doi.org/10.1017/S1431927606060090.

[31] X. Wang, S. Gao, E. Jain, B. Gaskey, M. Seita, Measuring crystal orientation from etched surfaces via directional reflectance microscopy, J. Mater. Sci. 55 (2020) 11669–11678. https://doi.org/10.1007/s10853-020-04734-z.